

# Grand Canonical Monte Carlo Simulations of the $^{129}\text{Xe}$ NMR Line Shapes of Xenon Adsorbed in $(\pm)\text{-}[\text{Co}(\text{en})_3]\text{Cl}_3$

Devin N. Sears,<sup>†</sup> Roderick E. Wasylishen,<sup>\*,†</sup> and Takahiro Ueda<sup>‡</sup>

Department of Chemistry, University of Alberta, Gunning-Lemieux Chemistry Centre, Edmonton, AB, Canada, T6G 2G2, and Department of Chemistry, Graduate School of Sciences, Osaka University, Toyonaka, Osaka, 560-0043, Japan

Received: March 16, 2006; In Final Form: April 11, 2006

The  $^{129}\text{Xe}$  NMR line shapes of xenon adsorbed in the nanochannels of the  $(\pm)\text{-}[\text{Co}(\text{en})_3]\text{Cl}_3$  ionic crystal have been calculated by grand canonical Monte Carlo (GCMC) simulations. The results of our GCMC simulations illustrate their utility in predicting  $^{129}\text{Xe}$  NMR chemical shifts in systems containing a transition metal. In particular, the nanochannels of  $(\pm)\text{-}[\text{Co}(\text{en})_3]\text{Cl}_3$  provide a simple, yet interesting, model system that serves as a building block toward understanding xenon chemical shifts in more complex porous materials containing transition metals. Using only the Xe–C and Xe–H potentials and shielding response functions derived from the Xe@CH<sub>4</sub> van der Waals complex to model the interior of the channel, the GCMC simulations correctly predict the  $^{129}\text{Xe}$  NMR line shapes observed experimentally (Ueda, T.; Eguchi, T.; Nakamura, N.; Wasylishen, R. E. *J. Phys. Chem. B* **2003**, *107*, 180–185). At low xenon loading, the simulated  $^{129}\text{Xe}$  NMR line shape is axially symmetric with chemical-shift tensor components  $\delta_{\parallel} = 379$  ppm and  $\delta_{\perp} = 274$  ppm. Although the simulated isotropic chemical shift,  $\delta_{\text{iso}} = 309$  ppm, is overestimated, the anisotropy of the chemical-shift tensor is correctly predicted. The simulations provide an explanation for the observed trend in the  $^{129}\text{Xe}$  NMR line shapes as a function of the overhead xenon pressure:  $\delta_{\perp}$  increased from 274 to 292 ppm, while  $\delta_{\parallel}$  changed by only 3 ppm over the entire xenon loading range. The overestimation of the isotropic chemical shifts is explained based upon the results of quantum mechanical  $^{129}\text{Xe}$  shielding calculations of xenon interacting with an isolated  $(\pm)\text{-}[\text{Co}(\text{en})_3]\text{Cl}_3$  molecule. The xenon chemical shift is shown to be reduced by about 12% going from the Xe@[Co(en)<sub>3</sub>]Cl<sub>3</sub> van der Waals complex to the Xe@C<sub>2</sub>H<sub>6</sub> fragment.

## 1. Introduction

With the rapid expansion of the nanotechnology field, new and interesting porous materials are continually being reported.<sup>1–3</sup> One such example is the class of materials referred to as metal organic frameworks (MOFs),<sup>4–24</sup> which are transition-metal complexes that are highly porous and have shown potential for hydrogen storage.<sup>25–27</sup> The high porosity of these nanomaterials makes the use of  $^{129}\text{Xe}$  nuclear magnetic resonance (NMR) ideal for the characterization of their internal volumes and adsorption behaviors because of the extreme sensitivity of the  $^{129}\text{Xe}$  chemical shift to the local environment in which the xenon finds itself.<sup>28–31</sup> Porous transition-metal complexes present new challenges in the interpretation and understanding of  $^{129}\text{Xe}$  NMR spectra arising from adsorbed xenon. Previously,  $^{129}\text{Xe}$  NMR has been utilized in investigations of inorganic materials such as zeolites and molecular sieves,<sup>32–43</sup> and recent reports have demonstrated its applicability in the study of organic systems such as dipeptide molecular crystals,<sup>44</sup> organic molecular crystals,<sup>45</sup> cryptophane cages,<sup>46–51</sup> and calixarenes.<sup>52</sup> In this investigation, we provide a theoretical examination of the  $^{129}\text{Xe}$  NMR line shapes arising from Xe adsorbed in the channels of the ionic crystal  $(\pm)\text{-}[\text{Co}(\text{en})_3]\text{Cl}_3$ . This prototypical transition-metal complex provides a well-defined system that serves as a first step toward understanding the  $^{129}\text{Xe}$  NMR spectra of xenon

adsorbed in porous transition-metal complexes. Such a system will help to decipher what elements are essential in a model system to accurately simulate the experimental NMR spectra.

Previous experimental studies carried out by Ueda et al.<sup>53</sup> have shown that the  $^{129}\text{Xe}$  NMR line shape resulting from xenon adsorbed in the channels of anhydrous  $(\pm)\text{-}[\text{Co}(\text{en})_3]\text{Cl}_3$  is axially symmetric. Only minor changes were observed in the  $^{129}\text{Xe}$  NMR line shape as a function of overhead xenon pressure, up to 6.5 MPa, quite unlike the typical line shape changes observed for Xe in other one-dimensional channels as a function of loading.<sup>44,45</sup> It is this curious and unusual behavior of the  $^{129}\text{Xe}$  NMR line shape as a function of overhead xenon pressure that led us to carry out grand canonical Monte Carlo (GCMC) simulations of xenon adsorbed in the channels of  $(\pm)\text{-}[\text{Co}(\text{en})_3]\text{Cl}_3$ .

## 2. The Model

Shown in Figure 1 is the X-ray crystal structure of  $(\pm)\text{-}[\text{Co}(\text{en})_3]\text{Cl}_3$ .<sup>54</sup> The first reports of the  $(\pm)\text{-}[\text{Co}(\text{en})_3]\text{Cl}_3$  crystal structure were of the hydrated form;<sup>55,56</sup> however, the previously reported  $^{129}\text{Xe}$  NMR experiments were performed on dehydrated samples,<sup>53</sup> so we used the X-ray structure of the dehydrated form as a starting point in generating our simulation model. The space group for the dehydrated crystal is trigonal,  $P\bar{3}c1$ , containing four formula units. Figure 1a presents a view down the crystallographic *c*-axis of the unit cell while Figure 1b depicts the crystallographic *c*-axis in the plane of the page. The unit cell parameters are  $a = 10.8119 \pm 0.0004$  Å and

\* To whom correspondence should be addressed. E-mail: roderick.wasylishen@ualberta.ca.

<sup>†</sup> University of Alberta.

<sup>‡</sup> Osaka University.

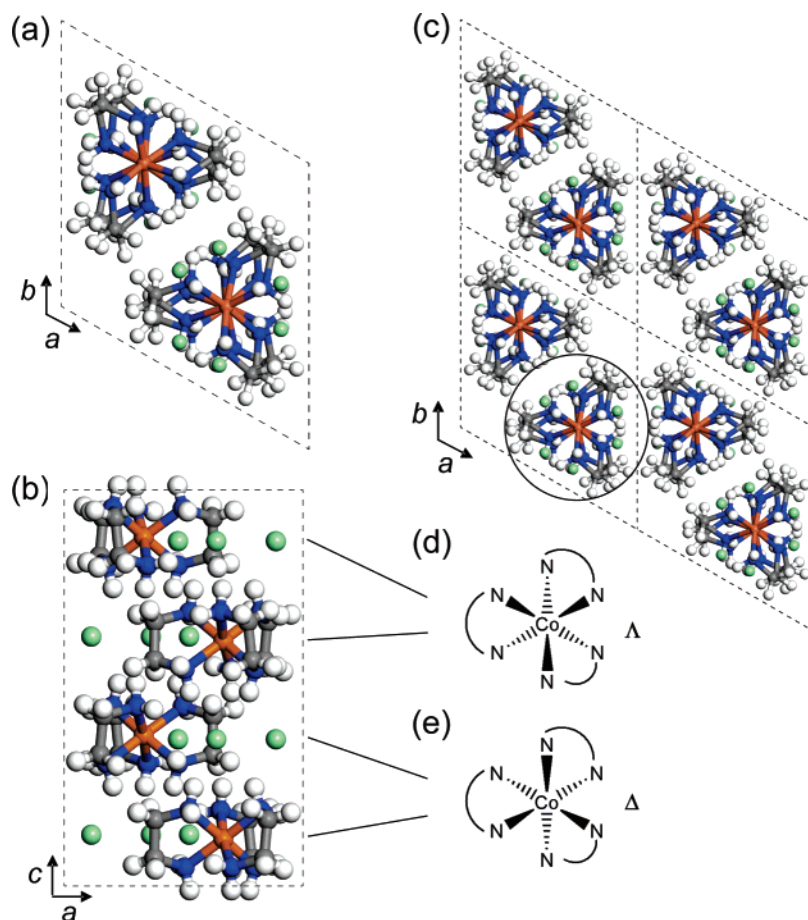


**Figure 1.** The structure of dehydrated ( $\pm$ )-[Co(en)<sub>3</sub>]Cl<sub>3</sub> determined by X-ray diffraction.<sup>54</sup> The unit cell viewed along the crystallographic *c*-axis (a) shows the stack arrangement of the ( $\pm$ )-[Co(en)<sub>3</sub>]<sup>3+</sup> cations along the *c*-axis. The four unique ( $\pm$ )-[Co(en)<sub>3</sub>]<sup>3+</sup> cations are shown in panel b. The channel formed by four adjacent unit cells is shown in panel c with an individual stack of ( $\pm$ )-[Co(en)<sub>3</sub>]<sup>3+</sup> cations circled. The  $\Lambda$  and  $\Delta$  isomers of the [Co(en)<sub>3</sub>]<sup>3+</sup> cation are pictured in graphic d and graphic e, respectively.

$c = 15.5351 \pm 0.001$  Å. The diffraction data for this structure were collected at  $-80$  °C. As shown in Figure 1c, the ionic crystal possesses a one-dimensional channel along the *c*-axis formed by hexagonal close-packing of the ( $\pm$ )-[Co(en)<sub>3</sub>]<sup>3+</sup> cations. The individual ( $\pm$ )-[Co(en)<sub>3</sub>]<sup>3+</sup> cations are arranged within the crystal in stacks, one particular stack is circled in Figure 1c. There are two separate stacks per unit cell. The stacks of ( $\pm$ )-[Co(en)<sub>3</sub>]<sup>3+</sup> cations crystallize such that the stereoisomers of the [Co(en)<sub>3</sub>]<sup>3+</sup> cation (denoted as  $\Lambda$  or  $\Delta$ , see Figure 1d and 1e) are repeated periodically. Specifically, the units arrange in an alternating  $-\Lambda-\Delta-\Lambda-\Delta-\Lambda-\Delta-$  fashion down a single stack which is parallel to the crystallographic *c*-axis. Two adjacent stacks are offset along the crystallographic *c*-axis by  $c/4$ . For a particular channel within the crystal, the effect of this packing is that the resulting channel is layered with three ( $\pm$ )-[Co(en)<sub>3</sub>]<sup>3+</sup> cations per crystallographic *ab* plane situated radially from the axis of the channel,  $120^\circ$  apart. All cations within a particular layer have the same stereochemistry, which results in a  $-\Lambda-\Lambda-\Delta-\Delta-\Lambda-\Lambda-\Delta-\Delta-$  layering pattern in the *ab* plane of the crystal. The orientation of the three ( $\pm$ )-[Co(en)<sub>3</sub>]<sup>3+</sup> cations in every second layer of the channel is rotated about the channel axis by  $60^\circ$  with respect to the layer above. The result of this specific packing of the ( $\pm$ )-[Co(en)<sub>3</sub>]<sup>3+</sup> cations is a nonuniform channel volume in which guest molecules can adsorb. For example, the cations in adjacent layers of the same stereochemistry (i.e.,  $-\Lambda-\Lambda-$  or  $-\Delta-\Delta-$ ) are oriented with respect to one another such that the methylene groups of the ethylenediamine ligands have their two hydrogens pointing toward either side of the channel axis. In this

configuration, an imaginary line drawn from the center of the channel to the carbon of the methylene group would nearly bisect the H–C–H bond angle of the CH<sub>2</sub> moiety. In contrast, the cations in adjacent layers of different stereochemistry (i.e.,  $-\Lambda-\Delta-$  or  $-\Delta-\Lambda-$ ) are oriented with respect to one another such that the CH<sub>2</sub> groups have one hydrogen atom directed toward the channel axis. That is, the C–H bond vector of the CH<sub>2</sub> group points toward the center of the channel. The overall result of the layered pattern of stereoisomers along the channel axis is that the channel is wider at some points along the channel axis and narrower or pinched at others. The effect of this pinching is the formation of discrete voids along the channel axis approximately 4.0 Å in diameter with constrictions roughly 3.7 Å in diameter separating adjacent voids.

The NMR experiments were conducted at room temperature, whereas the X-ray crystal structure was collected at  $-80$  °C. The higher temperature at which the <sup>129</sup>Xe NMR experiments were conducted is likely to result in some conformational disorder in the ethylenediamine ligands of the cobalt complexes. To prepare a model system which allows for the possibility of disorder in the NMR sample, we have performed molecular dynamics (MD) simulations on a periodic  $2 \times 2 \times 3$  supercell of ( $\pm$ )-[Co(en)<sub>3</sub>]Cl<sub>3</sub>, initially in the configuration revealed by X-ray diffraction at  $-80$  °C. A 100 ps MD annealing simulation was carried out in 1 fs time steps. First, the supercell was subjected to an initial 10 ps MD simulation at 300 K. Next, a series of 10 ps simulations were carried out in 50 K increments from 300 up to 500 K and then back down to 300 K. The universal force field<sup>57–60</sup> (UFF) was employed in these simula-

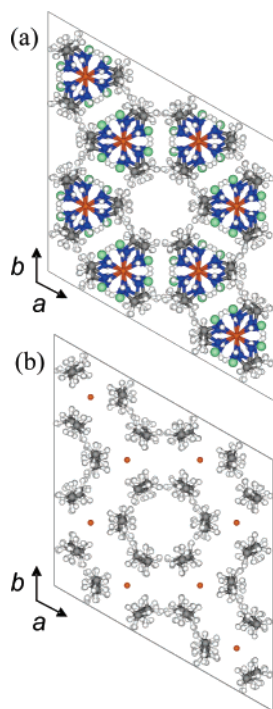


**Figure 2.** (a) The  $2 \times 2 \times 3$  supercell of  $(\pm)\text{-}[\text{Co}(\text{en})_3]\text{Cl}_3$  resulting from the molecular dynamics simulated annealing procedure discussed in the text. (b) The  $2 \times 2 \times 3$  supercell of model 1 used in the GCMC simulations. The N and H atoms of the  $\text{NH}_2$  groups have been removed and replaced with H atoms. The Co positions are retained as dummy atoms to prevent xenon from occupying the vacant lattice positions during the GCMC simulations.

tions because of the presence of the transition metal and the fact that the UFF has been parametrized for the entire periodic table. The cell parameters of the supercell and the positions of the Co and N atoms were fixed in the MD simulations. A final MD simulation of 50 ps at 300 K resulted in the structure used in the GCMC simulations, shown in Figure 2a.

Decorating the interior of the channel are the aliphatic methylene groups of the ethylenediamine ligands, as can be seen in Figure 2a. The aliphatic nature of the channel cross section suggests that the xenon will only be exposed to the ethylene unit of the ethylenediamine ligand; we therefore propose that the xenon energetics and shielding response can be simulated using the simpler xenon–methane system as a starting point. In other words, both the potential function and the shielding response functions for Xe–C and Xe–H are taken to be the same as that found for the Xe– $\text{CH}_4$  system. One way to do this is to replace each  $\text{H}_2\text{NCH}_2\text{CH}_2\text{NH}_2$  ligand with  $\text{HCH}_2\text{CH}_2\text{H}$  thereby truncating the  $(\pm)\text{-}[\text{Co}(\text{en})_3]\text{Cl}_3$  complex, resulting in the structure shown in Figure 2b. The substitution of the xenon–methane interactions for Xe interacting with the aliphatic groups decorating the inner surface of a nanochannel was first demonstrated in simulations of  $^{129}\text{Xe}$  NMR line shapes in dipeptide nanochannels.<sup>44</sup> The representation of the channel by only the interior  $\text{CH}_2$  groups, represented as an ethane molecule, will be denoted as model 1. As shown in Figure 2b, the positions of the cobalt atoms have been retained in model 1. Dummy atoms are assigned to the Co positions during the simulations to prevent xenon from occupying space within the unit cell previously occupied by cobalt or nitrogen atoms. The chloride ions were omitted in model 1, as were the  $\text{NH}_2$  groups. This model neglects the effects of the chlorine, nitrogen, or cobalt electrons on the intermolecular xenon chemical shift arising from both primary interactions with the xenon atom and secondary

interactions communicated to the xenon through the  $\sigma$  bonding to the  $\text{CH}_2$  groups of the ethylenediamine in the case of nitrogen and cobalt. The ability of the simple Xe– $\text{CH}_4$  response system to predict the correct  $^{129}\text{Xe}$  NMR line shapes in the hydrophobic nanochannels of dipeptides suggests that it will also work in the case of Xe in the  $(\pm)\text{-}[\text{Co}(\text{en})_3]\text{Cl}_3$  channels, which have similar aliphatic moieties lining its channel interior.

### 3. GCMC Simulations

The use of GCMC simulations in conjunction with the dimer–tensor model<sup>61,62</sup> to simulate  $^{129}\text{Xe}$  NMR line shapes has been successfully applied to xenon adsorbed in a wide variety of systems ranging from aluminosilicates<sup>61,63</sup> and aluminophosphates<sup>61,64</sup> to dipeptide nanochannels<sup>44</sup> and clathrate hydrates.<sup>65,66</sup> The extension of the GCMC simulations to transition-metal complexes is a natural extension of these previous simulations. The implementation of the GCMC simulations in conjunction with the dimer–tensor model relies on two components: first, a suitable set of potential energy functions describing the interaction of the adsorbed xenon atoms with the host material and, second, a set of dimer–tensor shielding functions describing the xenon shielding response as a function of the pairwise additive interaction of the adsorbed xenon atoms with the individual atoms of the host material.

The elements of the GCMC technique that we have employed are described by Allen and Tildesley,<sup>67</sup> and the calculation of average  $^{129}\text{Xe}$  NMR chemical shifts by GCMC methods was first reported by Jameson et al.<sup>68,69</sup> For the simulations carried out in this study, 3D periodic boundary conditions<sup>67</sup> were applied to simulation boxes composed of  $2 \times 2 \times 3$  unit cells. The Mezei cavity-biased sampling<sup>70</sup> scheme in conjunction with the standard Norman–Filinov method<sup>71</sup> was implemented within the GCMC simulations to ensure efficient exploration of configuration space. Each GCMC simulation was allowed to come to equilibrium over 100 000 cycles after which 1 000 000 GCMC cycles were completed to simulate the averaged  $^{129}\text{Xe}$  NMR line shape with block averages collected every 100 000 cycles.

The potentials used in the GCMC simulations to model xenon interacting with the  $\text{CH}_2$  groups of the  $(\pm)\text{-}[\text{Co}(\text{en})_3]\text{Cl}_3$  channel have a Maitland–Smith functional form, described by

$$V = \epsilon \left\{ \left( \frac{6}{n-6} \right) \bar{r}^{-n} - \left( \frac{n}{n-6} \right) \bar{r}^{-6} \right\} \quad (1)$$

where  $n$  is allowed to vary according to  $n = m + \gamma(\bar{r} - 1)$ , with  $\bar{r} = r/r_{\min}$ . The parameters used were those of the Xe– $\text{CH}_4$  system;<sup>72</sup> specifically  $r_{\min} = 4.0047 \text{ \AA}$ ,  $\epsilon = 141.52 \text{ K}$ ,  $\gamma = 9.5$ , and  $m = 13$  for the Xe–C interaction and  $r_{\min} = 3.671 \text{ \AA}$ ,  $\epsilon = 78.235 \text{ K}$ ,  $\gamma = 9.5$ , and  $m = 13$  for the Xe–H interactions. The Xe–Xe potential parameters are a fit to the Aziz–Slaman empirical potential.<sup>73</sup> To prevent xenon from exploring space vacated by the removal of the Co and  $\text{NH}_2$  groups from the lattice, a dummy atom was placed at the position of the Co atoms. The same Maitland–Smith potential was applied to these dummy atoms with a well depth,  $\epsilon$ , of 0 and an  $r_{\min}$  of  $4.0 \text{ \AA}$  resulting in a particle with no attractive force to the xenon and occupying the interchannel voids. The potential functions used in the GCMC simulations were cut-and-shifted in the usual manner<sup>67</sup> with a cutoff radius equal to half the length of the shortest side of the simulation box.

The dimer–tensor algorithm is briefly described here; the complete derivation of the model and detailed discussion can be found in ref 61. The basic tenet of the dimer–tensor model is that each symmetric magnetic shielding tensor component



of the  $J$ th xenon atom at a particular Cartesian position ( $x, y, z$ ) within the host material composed of atoms ( $A_i$ ) can be expressed in terms of a pairwise additive sum of contributions from the shielding tensor components of the  $\text{Xe}_J\text{--}A_i$  dimers. The perpendicular and parallel components of the nuclear magnetic shielding tensor,  $\sigma_\perp$  and  $\sigma_\parallel$ , of a single  $\text{Xe}_J\text{--}A_i$  dimer can be approximated by a general mathematical expression which is a function of the internuclear separation between  $\text{Xe}_J$  and  $A_i$  ( $r_{\text{Xe}_J\text{--}A_i}$ ):

$$\sigma(r_{\text{Xe}_J\text{--}A_i}) - \sigma(\text{free Xe atom}) = \sum_i a_6 r_{\text{Xe}_J\text{--}A_i}^{-6} + a_8 r_{\text{Xe}_J\text{--}A_i}^{-8} + a_{10} r_{\text{Xe}_J\text{--}A_i}^{-10} + a_{12} r_{\text{Xe}_J\text{--}A_i}^{-12} \quad (2)$$

where  $a_6, \dots, a_{12}$  are coefficients resulting from a least-squares fit to quantum mechanical calculations of the  $\text{Xe}_J\text{--}A_i$  dimer (for a detailed discussion of this fitting procedure see ref 49). The functional form expressed in eq 2 is used in the fit of both dimer shielding tensor components,  $\sigma_\perp$  and  $\sigma_\parallel$ , to the quantum mechanically calculated  $^{129}\text{Xe}$  shielding tensors in various configurations of a suitable model system for shielding response. This results in two sets of fitting coefficients for each unique xenon dimer. For example, the end result in fitting the quantum mechanical calculations of the  $\text{Xe}\text{--}\text{CH}_4$  shielding surface was the four sets of coefficients  $\sigma_\perp(\text{Xe}\text{--}\text{C})$ ,  $\sigma_\parallel(\text{Xe}\text{--}\text{C})$ ,  $\sigma_\perp(\text{Xe}\text{--}\text{H})$ , and  $\sigma_\parallel(\text{Xe}\text{--}\text{H})$ . The contribution of the  $i$ th atom to the total shielding tensor of the  $J$ th xenon in a particular configuration can be expressed in the Cartesian frame of the simulation box as follows for the diagonal elements:

$$\sigma_{xx} = [(x_i - x_J)/r_{ij}]^2 \sigma_\parallel + \{[(y_i - y_J)/r_{ij}]^2 + [(z_i - z_J)/r_{ij}]^2\} \sigma_\perp \quad (3)$$

and

$$1/2(\sigma_{xy} + \sigma_{yx}) = [(x_i - x_J)/r_{ij}][(y_i - y_J)/r_{ij}](\sigma_\parallel - \sigma_\perp) \quad (4)$$

for the off-diagonal elements, where  $x_i$  and  $x_J$  are the Cartesian positions of the  $i$ th host atom and the  $J$ th xenon atom,  $r_{ij}$  is the internuclear vector between atoms  $i$  and  $J$ , and  $\sigma_\perp$  and  $\sigma_\parallel$  are the perpendicular and parallel components of the shielding tensor for the  $\text{Xe}_J\text{--}A_i$  dimer. Terms such as these for all six unique components of the symmetric shielding tensor are summed over all  $i$  atoms in the surrounding host lattice. Additionally, all other xenon atoms ( $\text{Xe}_K$ ) within the vicinity of  $\text{Xe}_J$  are included in the summation. The dimer–tensor shielding functions used in the simulations performed in this study are those obtained by a fit to the  $\text{Xe}\text{--}\text{CH}_4$  shielding surface.<sup>74</sup>

In an external magnetic field,  $\mathbf{B}_0$ , oriented in an arbitrary direction with respect to the Cartesian frame of the simulation box, described by the angles  $\theta$  and  $\phi$ , the observable magnetic shielding response can be expressed as<sup>75,76</sup>

$$\sigma_{\mathbf{B}_0}(\theta, \phi) = \sigma_{xx} \sin^2 \theta \cos^2 \phi + \sigma_{yy} \sin^2 \theta \sin^2 \phi + \sigma_{zz} \cos^2 \theta + 1/2(\sigma_{xy} + \sigma_{yx}) \sin^2 \theta \sin 2\phi + 1/2(\sigma_{xz} + \sigma_{zx}) \sin 2\theta \cos \phi + 1/2(\sigma_{yz} + \sigma_{zy}) \sin 2\theta \sin \phi \quad (5)$$

where  $\sigma_{\mathbf{B}_0}(\theta, \phi)$  is the projection of the symmetric part of the magnetic shielding tensor along  $\mathbf{B}_0$ . For polycrystalline samples, such as those examined in this study, all possible orientations of the crystallite with respect to  $\mathbf{B}_0$  are present within the sample. Thus, to simulate the  $^{129}\text{Xe}$  NMR spectra of polycrystalline samples, the GCMC simulations are carried out within a fixed

frame (the Cartesian frame of the simulation box) while  $\mathbf{B}_0$  is reoriented over all  $(\theta, \phi)$  space. For each accepted configuration within the GCMC simulation,  $\mathbf{B}_0$  is oriented in 580 unique  $(\theta, \phi)$  orientations chosen uniformly over the surface of a sphere to ensure uniform sampling of all possible orientations. Polycrystalline powder line shapes result when the ensemble averages of eq 5,  $\langle \sigma_{\mathbf{B}_0}(\theta, \phi) \rangle$ , are binned into a histogram. The frequency associated with the center of each bin of the coarse histogram resulting from the Monte Carlo simulations is smoothed by a Lorentzian function of a fixed width to generate the  $^{129}\text{Xe}$  NMR spectrum. The bin width used in this study was 0.625 ppm, and a Lorentzian line width of 0.5 ppm was used on peaks in the histogram corresponding to less than five consecutively populated bins in the histogram and 1.5 ppm for all others. The dimer–tensor shielding functions used within the GCMC simulations were cut-and-shifted in an analogous manner as the potential functions.

The relationship between shielding,  $\sigma$ , and chemical shift,  $\delta$ , is defined as

$$\delta_i = \frac{\sigma_{\text{ref}} - \sigma_i}{1 - \sigma_{\text{ref}}} \approx \sigma_{\text{ref}} - \sigma_i \quad (6)$$

where  $\sigma_{\text{ref}}$  is the shielding of the reference, in this case the free xenon atom, and  $\sigma_i$  is the shielding of the xenon of interest. In the case of intermolecular xenon shieldings, the neglect of the denominator in the first part of eq 6 introduces less than 1% error in the corresponding chemical shift; therefore, the approximation in the second part of eq 6 was used.

#### 4. Quantum Mechanical Calculations

To critically evaluate the magnitude of the errors incurred by using model 1, we have carried out a series of quantum mechanical calculations of xenon interacting with various fragments of the  $(\pm)\text{--}[\text{Co}(\text{en})_3]\text{Cl}_3$  complex. The fragments chosen were ethane, ethylenediamine, and an isolated  $[\text{Co}(\text{en})_3]\text{Cl}_3$  complex. This set of fragment molecules, building up from the ethane molecule to the  $(\pm)\text{--}[\text{Co}(\text{en})_3]\text{Cl}_3$  complexes making up the channel, allowed us to assess the effects of the more complex systems' electronic structure on the xenon shielding response.

Nuclear magnetic shielding calculations were carried out using the Parallel Quantum Solutions (PQS) software package of Pulay and co-workers.<sup>77</sup> All shieldings were calculated with density-functional theory (DFT) using gauge including atomic orbitals (GIAO)<sup>78–80</sup> and the three-parameter hybrid functional of Becke (B3LYP).<sup>81</sup> The basis set of Partridge and Feagri<sup>82</sup> with additional polarization functions of Bishop and Cybulski<sup>83</sup> was used for xenon; the 6-311G\*\* basis set was employed for all C, N, and H atoms, and the 6-31G\* basis set was applied to the Co and Cl atoms.

The xenon–methane shielding surface was calculated at 70 unique configurations with the xenon atom approaching the  $\text{CH}_4$  molecule along the three unique symmetry axes of the  $\text{CH}_4$  molecule: first, an approach of the xenon atom collinear with one H–C bond; second, the xenon approach is perpendicular to the tetrahedral face of the  $\text{CH}_4$  molecule; and the third with xenon approaching perpendicular to an edge of the  $\text{CH}_4$  tetrahedron.<sup>74</sup> The resulting shielding values were fit to the functional form of eq 2.

The structures of the  $\text{C}_2\text{H}_6$  and  $\text{H}_2\text{NCH}_2\text{CH}_2\text{NH}_2$  molecules were obtained by a full geometry optimization of the two molecules at the B3LYP/6-311G\*\* level. The geometry of the  $[\text{Co}(\text{en})_3]\text{Cl}_3$  complex was obtained from the X-ray crystal

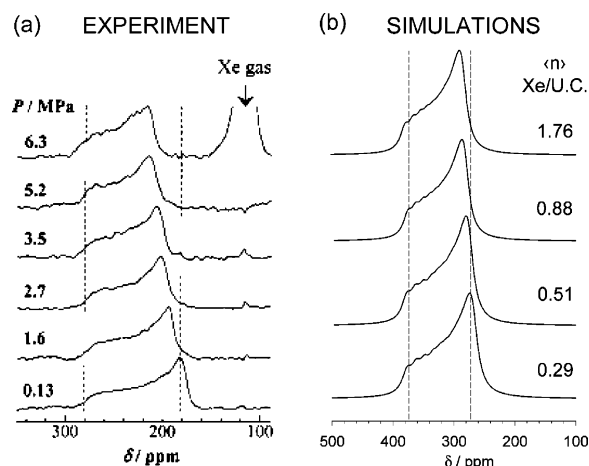


**Figure 3.** The  $^{129}\text{Xe}$  NMR line shapes of xenon adsorbed in the channels of  $(\pm)\text{-}[\text{Co}(\text{en})_3]\text{Cl}_3$  are shown as a function of the overhead xenon pressure: (a) experimental spectra; (b) simulated spectra. The simulated spectra (b) are shown as a function of xenon loading. (The experimental spectra are reprinted from ref 53. Copyright 2003 American Chemical Society.)

structure of the dehydrated complex described earlier.<sup>54</sup> The A isomer was arbitrarily chosen and the proton positions of the ethylenediamine ligands were optimized at the B3LYP/6-311G\*\* level prior to the magnetic shielding calculations. The positions of the three chloride anions were also taken from the X-ray structure and are located on the opposite side of the  $[\text{Co}(\text{en})_3]^{3+}$  cation relative to the line of approach of the xenon atom. The configurations of the xenon atom relative to the three molecules were chosen such that the xenon atom approached an edge of the tetrahedron formed by a  $\text{CH}_3$  group of the ethane molecule and the analogous tetrahedral edges of the other two molecules. This particular set of xenon configurations was chosen because it represents configurations that were frequently sampled during the GCMC simulations and are therefore most representative of the average  $^{129}\text{Xe}$  shielding in the channel.

For the shielding calculations of  $\text{Xe}@\text{[Co(en)}_3\text{]Cl}_3$  complexes, convergence of the variational wave functions was problematic due to the highly ionic nature of the  $[\text{Co}(\text{en})_3]\text{Cl}_3$  molecule. To circumvent this problem, a low-level calculation of the complex at the DFT/B3LYP level with a uniform STO-3G basis set was first carried out using the quadratically convergent self-consistent field (SCF) procedure<sup>84</sup> rather than the standard direct inversion of the iterative subspace (DIIS) method.<sup>85</sup> The resulting variational wave function then provides the initial guess in a subsequent single-point calculation at the DFT/B3LYP level with the 6-311G\*\* basis set on all C, N, and H atoms, with the 6-31G\* basis set on the Co and Cl atoms, and with the xenon assigned an STO-3G basis. In a final step, the xenon shielding calculation was carried out using the previous step as an initial guess at the DFT/B3LYP level with the 6-311G\*\* basis set on all C, N, and H atoms and with the 6-31G\* basis set on the Co and Cl atoms, and the xenon was then assigned the full 240 basis functions described previously. The usual DIIS SCF method was employed in the second and final iterations.

## 5. Results and Discussions

Shown in Figure 3a are the experimentally observed  $^{129}\text{Xe}$  NMR line shapes for xenon adsorbed in  $(\pm)\text{-}[\text{Co}(\text{en})_3]\text{Cl}_3$ , taken from ref 53. The spectrum collected at low overhead xenon pressure (0.13 MPa) shows that the observed line shapes correspond to an axially symmetric line shape with  $\delta_{\parallel} = 280$  and  $\delta_{\perp} = 180$  ppm. In this case,  $\delta_{\parallel}$  is the chemical shift when

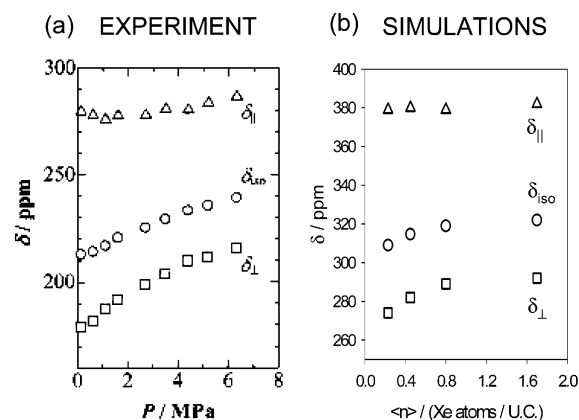


**Figure 4.** The dependence of the  $^{129}\text{Xe}$  chemical-shift tensor on xenon loading in the channels of  $(\pm)\text{-}[\text{Co}(\text{en})_3]\text{Cl}_3$ : (a) the experimental data; (b) the simulated results. (The experimental data are reprinted with permission from ref 53. Copyright 2003 American Chemical Society.)

the external magnetic field,  $\mathbf{B}_0$ , is oriented along the channel axis, and  $\delta_{\perp}$  is the chemical shift when  $\mathbf{B}_0$  is aligned perpendicular to the channel axis. By convention, the isotropic chemical shift is defined as  $\delta_{\text{iso}} = (1/3)(\delta_{\parallel} + 2\delta_{\perp})$ , and here we define the chemical-shift anisotropy,  $\Delta\delta = \delta_{\parallel} - \delta_{\perp}$ . From Figure 3a, the anisotropy in the  $^{129}\text{Xe}$  NMR line shape obtained at the lowest overhead xenon pressure is approximately 100 ppm.

As the overhead xenon pressure is increased, the  $^{129}\text{Xe}$  chemical-shift tensor component perpendicular to the channel axis,  $\delta_{\perp}$ , increases, whereas the parallel component,  $\delta_{\parallel}$ , remains essentially unchanged. These results indicate that even at elevated overhead pressures of xenon gas, the xenon is unable to heavily load the lattice, a point clearly demonstrated in Figure 4a (also reprinted from ref 53), which depicts the change in the  $^{129}\text{Xe}$  shielding tensor components as a function of the overhead pressure of xenon gas. A decrease in the change of the  $\delta_{\perp}$  tensor component at higher xenon gas pressure,  $d\delta_{\perp}/dP$ , demonstrates that the maximum loading of the crystal lattice is being approached. The  $\delta_{\perp}$  chemical-shift tensor component is more sensitive to xenon loading because it is most influenced by xenon–xenon interactions within the channel; thus with more xenon adsorbed in the lattice, the xenon–xenon contribution to the total shielding tensor begins to dominate the  $^{129}\text{Xe}$  chemical-shift tensor as the average xenon–xenon distance is reduced. Usually, as xenon loading in a nanochannel increases, the  $^{129}\text{Xe}$  NMR line shape systematically changes such that the anisotropy,  $\Delta\delta$ , changes sign with a fortuitous isotropic line shape near the middle of the progression.<sup>62</sup> However, in this case, the sign of the anisotropy does not change, further supporting the point that the Xe–Xe interactions are somehow disabled by the host  $(\pm)\text{-}[\text{Co}(\text{en})_3]\text{Cl}_3$  lattice.

The  $^{129}\text{Xe}$  NMR line shapes calculated by GCMC simulations at various xenon loadings are shown in Figure 3b. The simulations of xenon in  $(\pm)\text{-}[\text{Co}(\text{en})_3]\text{Cl}_3$  do indeed reproduce the trend in the  $^{129}\text{Xe}$  NMR line shape as the xenon loading in the channel approaches two xenon atoms per unit cell. The average isotropic chemical shift,  $\delta_{\text{iso}}$ , simulated for the lowest xenon loading is 309 ppm and increases to 322 ppm at the highest xenon loading. Furthermore, the simulated  $^{129}\text{Xe}$  chemical-shift tensors as a function of xenon loading are in accord with experimental observations, with  $\delta_{\perp}$  increasing from 274 ppm at low xenon loading to 292 ppm at high xenon loading and  $\delta_{\parallel}$  remaining nearly constant around 379 ppm at low xenon loading and 382 ppm at the highest xenon loading. Figure 4 more clearly demonstrates that the trends in the calculated  $^{129}\text{Xe}$  chemical-shift tensor components compare favorably with

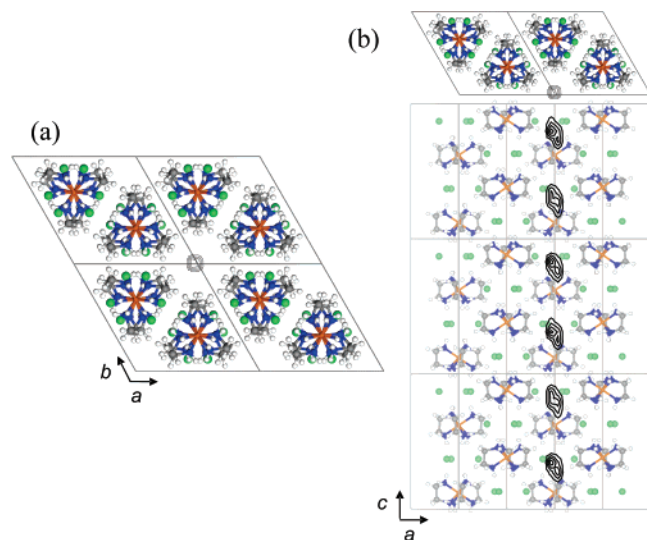


**Figure 5.** The one-body distribution of xenon in the channels of ( $\pm$ )-[Co(en)<sub>3</sub>]Cl<sub>3</sub>. Shown in panel a is the probability of finding a Xe atom in a particular plane perpendicular to the channel axis, also repeated at the top of panel b. Shown in panel b is the probability of finding a Xe atom in that particular plane parallel to the channel axis indicated by the truncated cross section. This clearly demonstrates xenon occupancy in discrete cavities along the channel, corresponding to every-other layer moving down the channel axis.

experiment, despite the fact that  $\delta_{\text{iso}}$  is overestimated by the GCMC simulations. In particular, the simulations properly predict that  $\delta_{\parallel}$  is almost invariant to xenon loading whereas  $\delta_{\perp}$  is found to be sensitive to the xenon loading, all the while maintaining a positive sign in the anisotropy. The results of the GCMC simulations demonstrate that model 1 provides essentially all the necessary contributions to the intermolecular xenon shielding tensor to reproduce the correct <sup>129</sup>Xe NMR line shape attributes.

In addition to the calculated <sup>129</sup>Xe NMR line shapes, the GCMC simulations generate Xe one-body distribution functions<sup>67</sup> providing detailed information about where the xenon atoms reside during the simulation. Shown in Figure 5 is the one-body distribution function from the GCMC simulations carried out at high xenon loading (1.756 xenon atoms per unit cell). The one-body distribution function has been overlaid on a cutaway of the ( $\pm$ )-[Co(en)<sub>3</sub>]Cl<sub>3</sub> structure to illustrate where the xenon atoms are distributed with respect to the channel during the simulation. It is clear that the xenon atoms reside in discrete volumes or pockets along the channel axis, with only one xenon atom occupying a single pocket even under conditions of high xenon loading. With two pockets per unit cell, these results indicate that the maximum xenon loading is two xenon atoms per unit cell. The one-body distribution function is consistent with the structural details of the channel imposed by the layered arrangement of the cation stereoisomers along the channel axis. Of particular interest is that the xenon resides between layers possessing the same stereochemistry ( $-\Delta-\Delta-$  or  $-\Delta-\Delta-$ ). This partitioning of the xenon occupancy is due to the arrangement of adjacent layers of similar or opposite stereochemistry as discussed in section 2 and limits the ability of the xenon atoms to interact with one another, thus dictating the change in the <sup>129</sup>Xe NMR line shape as a function of overhead xenon gas pressure. Despite the fact that the xenon atoms are not allowed to come in close contact with one another because of the structural morphology of the channel interior, one can see from Figure 5 that the one-body distribution indicates that a small fraction of the total occupancy is moving

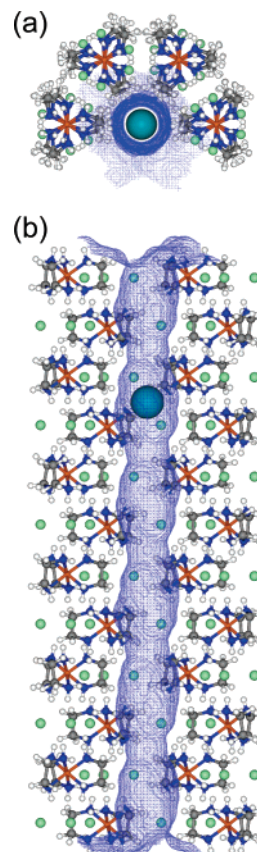


**Figure 6.** The solvent-accessible surface area of the nanochannel of a ( $\pm$ )-[Co(en)<sub>3</sub>]Cl<sub>3</sub> crystal: (a) a view down the channel axis with a xenon atom positioned in a high probability position in the channel; (b) a view of the surface parallel to the channel axis depicting the voids and restrictions present along the channel axis.

into regions of the channel where the xenon is not found at lower xenon loadings. Evidenced by the asymmetrical tail on the bottom right section of each discrete probability density along the channel axis, this asymmetry in the one-body distribution results in slightly shorter Xe–Xe distances being sampled during the simulation giving rise to a larger xenon–xenon contribution to  $\delta_{\perp}$ . The tail of the one-body distribution function helps to explain the change in  $\delta_{\parallel}$  at elevated overhead pressure. The  $\delta_{\parallel}$  component is largely determined by xenon interacting with channel atoms in the same plane as the xenon atom perpendicular to the channel axis. At elevated overhead xenon gas pressure, the xenon atoms begin to experience regions of channel constriction that brings the xenon atoms into closer proximity to the channel wall atoms. Such an interaction results in an increase in  $\delta_{\parallel}$ . The one-body distribution at high xenon occupancy clearly explains why the xenon–xenon interaction never becomes large enough to dominate the observed <sup>129</sup>Xe NMR line shape and reverse the sign of the xenon chemical-shift anisotropy.

To obtain a better visual image of the interior volume available to the xenon atom, a solvent accessible surface area map was generated for the ( $\pm$ )-[Co(en)<sub>3</sub>]Cl<sub>3</sub> channel. Figure 6 depicts the surface of the channel generated by rolling over the surface of the channel a spherical particle of 4.0 Å diameter, approximately the diameter of a xenon atom (the van der Waals radius of Xe is 2.16 Å<sup>86</sup>). The view down the channel axis shown in Figure 6a demonstrates how compact the channel is relative to the xenon atom which is shown as a green sphere at the center of the channel. Figure 6b results from a 90° rotation of Figure 6a into the page. As can be seen in Figure 6b, there



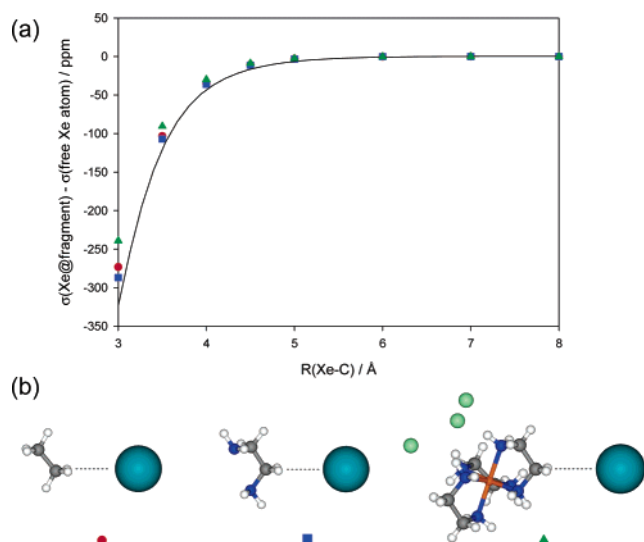


**Figure 7.** (a) Results of quantum mechanical magnetic shielding calculations for xenon interacting with ethane (●), ethylenediamine (■), and  $[\text{Co}(\text{en})_3]\text{Cl}_3$  (▲). The solid line represents the isotropic shielding function used in the GCMC simulations. Shown in panel b are the trajectories of xenon approaching ethane (●), ethylenediamine (■), and  $[\text{Co}(\text{en})_3]\text{Cl}_3$  (▲).

are voids along the channel axis. The constrictions formed by adjacent layers of opposite stereoisomers can also be seen in the surface shown in Figure 6b. The solvent-accessible surface area map is also consistent with the one-body distribution function resulting from the GCMC simulations.

The discrepancies between the simulated and experimentally observed  $^{129}\text{Xe}$  NMR line shapes are attributed to the fact that model 1 is approximate. We can begin to explain the deficiencies in model 1 by examining the results of quantum mechanical calculations that we have carried out on model fragments, shown in Figure 7a. Xenon magnetic shielding calculations were performed for Xe–R at various Xe–R separations along trajectories depicted in Figure 7b, where R = ethane, ethylenediamine, and  $[\text{Co}(\text{en})_3]\text{Cl}_3$ . These calculations show that as the model fragment becomes more complex the xenon chemical shift is modified. The solid line shown in Figure 7a is the isotropic dimer–tensor shielding function used in the GCMC simulations. Figure 7 demonstrates that the Xe@CH<sub>4</sub> dimer–tensor shielding functions used in the GCMC simulations overestimate the isotropic  $^{129}\text{Xe}$  chemical shift by approximately 12% for the Xe@[Co(en)<sub>3</sub>]Cl<sub>3</sub> complex (i.e., scaling the solid line in Figure 7 by 12% would result in a shielding response function that accurately describes the shielding calculations of Xe@[Co(en)<sub>3</sub>]Cl<sub>3</sub>). This change in the xenon shielding response indicates that the chemical-shift tensors calculated for xenon in the channels of (±)-[Co(en)<sub>3</sub>]Cl<sub>3</sub> by GCMC simulations, using the Xe@CH<sub>4</sub> dimer–tensor shielding functions, have been overestimated because the electronic structure which the methane molecule presents to the xenon nucleus is different from that for the [Co(en)<sub>3</sub>]Cl<sub>3</sub> molecule. Interestingly, one can see from Figure 7a that there is very little difference in the xenon shielding response to ethylenediamine compared to ethane. The xenon shielding response to ethylenediamine is slightly more deshielded than to ethane. On the other hand, the xenon shielding response to the [Co(en)<sub>3</sub>]Cl<sub>3</sub> molecule is clearly smaller in magnitude. This overestimation of the xenon chemical shift by the Xe@CH<sub>4</sub> dimer–tensor shielding functions helps account for the observed discrepancies between the calculated  $^{129}\text{Xe}$  NMR line shapes of xenon in (±)-[Co(en)<sub>3</sub>]Cl<sub>3</sub> and those obtained experimentally. The results of the quantum mechanical calculations are for an

isolated  $[\text{Co}(\text{en})_3]\text{Cl}_3$  molecule, whereas in the lattice it is assumed that there is an infinite number of  $[\text{Co}(\text{en})_3]\text{Cl}_3$  molecules. If we assume pairwise additivity of the xenon chemical shift, the presence of the extended lattice, in particular the nearest neighboring  $[\text{Co}(\text{en})_3]\text{Cl}_3$  molecules, will further compensate for the overestimation of the xenon chemical shift.

Of course, the intermolecular potential likewise arises from the electronic response of the xenon atom to its surrounding environment, and this too would be modified in an analogous way. These results indicate that to obtain quantitative agreement with experiment, a xenon shielding surface calculated in the presence of the entire transition-metal complex is necessary as well as a set of potential functions more appropriate than the Xe–CH<sub>4</sub> potentials. Although there is no direct interaction of the xenon atom with the cobalt atom, the electronic structure of the methylene groups which interacts directly with the Xe atom is clearly affected by the metal.

## 6. Conclusions

Grand canonical Monte Carlo simulations implementing the dimer–tensor model have been carried out to simulate the  $^{129}\text{Xe}$  NMR line shapes of xenon adsorbed in the ionic crystal of (±)-[Co(en)<sub>3</sub>]Cl<sub>3</sub> and provide insight into the adsorption behavior of xenon in (±)-[Co(en)<sub>3</sub>]Cl<sub>3</sub>. The GCMC simulations faithfully reproduce the observed changes in the  $^{129}\text{Xe}$  NMR line shape as a function of xenon loading within the channels. Furthermore, one-body distributions account for the observed trends in the  $^{129}\text{Xe}$  line shapes. Qualitatively, the morphology of the channel interior prevents the xenon from experiencing any significant interactions with other adsorbed xenon atoms.

The use of the Xe@CH<sub>4</sub> potentials and dimer–tensor shielding functions was sufficient in this model system to reproduce the experimentally observed trends in the  $^{129}\text{Xe}$  NMR line shape. More quantitative simulations will require reformulation of the potentials and dimer–tensor shielding surfaces for xenon interacting with the entire [Co(en)<sub>3</sub>]Cl<sub>3</sub> molecule. This is an important point to make because it suggests that designing a model system that presents an appropriate electronic structure to the Xe atom will be necessary for the interpretation of the experiments carried out on more complex frameworks containing transition metals. The ligand moieties which constitute the channel surface in this case serve as an initial test; however, when the transition metal is more exposed to the xenon atom (as is the case in the MOF systems), the metal has to be explicitly included in the model used for the quantum mechanical calculation of the Xe shielding response. Investigations of more complex examples involving transition-metal atoms are required to further investigate this point. One such example would be the porous metal–organic macrocycles<sup>88</sup> for which there is already experimental  $^{129}\text{Xe}$  NMR data available in the literature.<sup>89</sup>

**Acknowledgment.** We thank the Natural Sciences and Engineering Research Council of Canada, the Alberta Ingenuity Fund, and the University of Alberta for research grants and scholarships. D.N.S. is an Izaak Walton Killam Postdoctoral Fellow and R.E.W. is a Canada Research Chair in Physical Chemistry at the University of Alberta. The authors wish to thank Prof. C. J. Jameson at the University of Illinois at Chicago for graciously providing the GCMC simulation code and for helpful discussions.

## References and Notes

- (1) Rao, C. N. R.; Muller, A.; Ceetham, A. K., Eds. *The Chemistry of Nanomaterials: Synthesis, Properties and Applications*; Wiley-VCH: Weinheim, Germany, 2004.

- (2) Wilson, M. *Nanotechnology: Basic Science and Emerging Technologies*; Chapman and Hall/CRC: Boca Raton, FL, 2002.
- (3) Wolf, E. L. *Nanophysics and Nanotechnology: An Introduction to Modern Concepts in Nanoscience*; Wiley-VCH: Weinheim, Germany, 2004.
- (4) Chen, B.; Fronczek, F. R.; Maverick, A. W. *Inorg. Chem.* **2004**, *43*, 8209–8211.
- (5) de Lill, D. T.; Gunning, N. S.; Cahill, C. L. *Inorg. Chem.* **2005**, *44*, 258–266.
- (6) Ding, B.-B.; Weng, Y.-Q.; Mao, Z.-W.; Lam, C.-K.; Chen, X.-M.; Ye, B.-H. *Inorg. Chem.* **2005**, *44*, 8836–8845.
- (7) Evans, O. R.; Lin, W. *Inorg. Chem.* **2000**, *39*, 2189–2198.
- (8) Fan, J.; Sun, W.-Y.; Okamura, T.-a.; Tang, W.-X.; Ueyama, N. *Inorg. Chem.* **2003**, *42*, 3168–3175.
- (9) Fan, J.; Zhu, H.-F.; Okamura, T.-a.; Sun, W.-Y.; Tang, W.-X.; Ueyama, N. *Inorg. Chem.* **2003**, *42*, 158–162.
- (10) Halper, S. R.; Cohen, S. M. *Inorg. Chem.* **2005**, *44*, 486–488.
- (11) Prior, T. J.; Rosseinsky, M. J. *Inorg. Chem.* **2003**, *42*, 1564–1575.
- (12) Sudik, A. C.; Cote, A. P.; Yaghi, O. M. *Inorg. Chem.* **2005**, *44*, 2998–3000.
- (13) Zhao, B.; Yi, L.; Dai, Y.; Chen, X.-Y.; Cheng, P.; Liao, D.-Z.; Yan, S.-P.; Jiang, Z.-H. *Inorg. Chem.* **2005**, *44*, 911–920.
- (14) Eddaoudi, M.; Li, H.; Yaghi, O. M. *J. Am. Chem. Soc.* **2000**, *122*, 1391–1397.
- (15) Kim, J.; Chen, B.; Reineke, T. M.; Li, H.; Eddaoudi, M.; Moler, D. B.; O'Keeffe, M.; Yaghi, O. M. *J. Am. Chem. Soc.* **2001**, *123*, 8239–8247.
- (16) Li, Y.; Yang, R. T. *J. Am. Chem. Soc.*, ACS ASAP.
- (17) Li, H.; Eddaoudi, M.; Groy, T. L.; Yaghi, O. M. *J. Am. Chem. Soc.* **1998**, *120*, 8571–8572.
- (18) Lu, W.-G.; Su, C.-Y.; Lu, T.-B.; Jiang, L.; Chen, J.-M. *J. Am. Chem. Soc.* **2006**, *128*, 34–35.
- (19) Millward, A. R.; Yaghi, O. M. *J. Am. Chem. Soc.* **2005**, *127*, 17998–17999.
- (20) Rosi, N. L.; Kim, J.; Eddaoudi, M.; Chen, B.; O'Keeffe, M.; Yaghi, O. M. *J. Am. Chem. Soc.* **2005**, *127*, 1504–1518.
- (21) Rowsell, J. L. C.; Millward, A. R.; Park, K. S.; Yaghi, O. M. *J. Am. Chem. Soc.* **2004**, *126*, 5666–5667.
- (22) Rowsell, J. L. C.; Eckert, J.; Yaghi, O. M. *J. Am. Chem. Soc.* **2005**, *127*, 14904–14910.
- (23) Rowsell, J. L. C.; Yaghi, O. M. *J. Am. Chem. Soc.* **2006**, *128*, 1304–1315.
- (24) Skoulidas, A. I. *J. Am. Chem. Soc.* **2004**, *126*, 1356–1357.
- (25) Chen, B.; Eddaoudi, M.; Hyde, S. T.; O'Keeffe, M.; Yaghi, O. M. *Science* **2001**, *291*, 1021–1023.
- (26) Rosi, N. L.; Eckert, J.; Eddaoudi, M.; Vodak, D. T.; Kim, J.; O'Keeffe, M.; Yaghi, O. M. *Science* **2003**, *300*, 1127–1130.
- (27) Zhao, X.; Xiao, B.; Fletcher, A. J.; Thomas, K. M.; Bradshaw, D.; Rosseinsky, M. J. *Science* **2004**, *306*, 1012–1015.
- (28) Bartik, K.; Choquet, P.; Constantinesco, A.; Duhamel, G.; Fraissard, J.; Hyacinthe, J.-N.; Jokisaari, J.; Locci, E.; Lowery, T. J.; Luhmer, M.; Meersmann, T.; Moudrakovski, I. L.; Pavlovskaya, G. E.; Pierce, K. L.; Pines, A.; Ripmeester, J. A.; Telkki, V.-V.; Veeman, W. S. *Actual. Chim.* **2005**, *287*, 16–33.
- (29) Ratcliffe, C. I. *Annu. Rep. NMR Spectrosc.* **1998**, *36*, 123–221.
- (30) Springuel-Huet, M. A. *NATO Sci. Ser., II* **2002**, *76*, 255–266.
- (31) Springuel-Huet, M. A.; Bonardet, J. L.; Fraissard, J. *App. Nucl. Magn. Reson.* **1995**, *8*, 427–456.
- (32) Ratcliffe, C. I.; Ripmeester, J. A. *J. Am. Chem. Soc.* **1995**, *117*, 1445–1446.
- (33) Ripmeester, J. A. *J. Magn. Reson.* **1984**, *56*, 247–253.
- (34) Ripmeester, J. A.; Ratcliffe, C. I. *J. Phys. Chem.* **1990**, *94*, 7652–7656.
- (35) Larsen, R. G.; Shore, J.; Schmidt-Rohr, K.; Emsley, L.; Long, H.; Pines, A.; Janicke, M.; Chmelka, B. F. *Chem. Phys. Lett.* **1993**, *214*, 220–226.
- (36) Janicke, M.; Chmelka, B. F.; Larsen, R. G.; Shore, J.; Schmidt-Rohr, K.; Emsley, L.; Long, H.; Pines, A. *Stud. Surf. Sci. Catal.* **1994**, *84*, 519–526.
- (37) Ito, T.; Fraissard, J. *J. Chem. Phys.* **1982**, *76*, 5225–5229.
- (38) Ripmeester, J. A.; Ratcliffe, C. I. *J. Phys. Chem.* **1995**, *99*, 619–622.
- (39) Tersikh, V. V.; Moudrakovski, I. L.; Du, H.; Ratcliffe, C. I.; Ripmeester, J. A. *J. Am. Chem. Soc.* **2001**, *123*, 10399–10400.
- (40) De Menorval, L. C.; Raftery, D.; Liu, S. B.; Takegoshi, K.; Ryoo, R.; Pines, A. *J. Phys. Chem.* **1990**, *94*, 27–31.
- (41) Chmelka, B. F.; De Menorval, L. C.; Csencsits, R.; Ryoo, R.; Liu, S. B.; Radke, C. J.; Petersen, E. E.; Pines, A. *Stud. Surf. Sci. Catal.* **1989**, *48*, 269–278.
- (42) Chmelka, B. F.; Raftery, D.; McCormick, A. V.; De Menorval, L. C.; Levine, R. D.; Pines, A. *Phys. Rev. Lett.* **1991**, *66*, 580–583.
- (43) Chmelka, B. F.; Ryoo, R.; Liu, S. B.; De Menorval, L. C.; Radke, C. J.; Petersen, E. E.; Pines, A. *J. Am. Chem. Soc.* **1988**, *110*, 4465–4467.
- (44) Moudrakovski, I.; Soldatov, D. V.; Ripmeester, J. A.; Sears, D. N.; Jameson, C. J. *Proc. Natl. Acad. Sci. U.S.A.* **2004**, *101*, 17924–17929.
- (45) Meersmann, T.; Logan, J. W.; Simonutti, R.; Caldarelli, S.; Comotti, A.; Sozzani, P.; Kaiser, L. G.; Pines, A. *J. Phys. Chem. A* **2000**, *104*, 11665–11670.
- (46) Brotin, T.; Dutasta, J.-P. *Eur. J. Org. Chem.* **2003**, 973–984.
- (47) Han, S.-I.; Garcia, S.; Lowery, T. J.; Ruiz, E. J.; Seeley, J. A.; Chavez, L.; King, D. S.; Wemmer, D. E.; Pines, A. *Anal. Chem.* **2005**, *77*, 4008–4012.
- (48) Huber, J. G.; Dubois, L.; Desvaux, H.; Dutasta, J.-P.; Brotin, T.; Berthault, P. *J. Phys. Chem. A* **2004**, *108*, 9608–9615.
- (49) Sears, D. N.; Jameson, C. J. *J. Chem. Phys.* **2003**, *119*, 12231–12244.
- (50) Spence, M. M.; Rubin, S. M.; Dimitrov, I. E.; Ruiz, E. J.; Wemmer, D. E.; Pines, A.; Yao, S. Q.; Tian, F.; Schultz, P. G. *Proc. Natl. Acad. Sci. U.S.A.* **2004**, *98*, 10654–10657.
- (51) Spence, M. M.; Ruiz, E. J.; Rubin, S. M.; Lowery, T. J.; Winssinger, N.; Schultz, P. G.; Wemmer, D. E.; Pines, A. *J. Am. Chem. Soc.* **2004**, *126*, 15287–15294.
- (52) Dubes, A.; Moudrakovski, I. L.; Shahgaldian, P.; Coleman, A. W.; Ratcliffe, C. I.; Ripmeester, J. A. *J. Am. Chem. Soc.* **2004**, *126*, 6236–6237.
- (53) Ueda, T.; Eguchi, T.; Nakamura, N.; Wasylishen, R. E. *J. Phys. Chem. B* **2003**, *107*, 180–185.
- (54) Ueda, T.; Bernard, G. M.; McDonald, R.; Wasylishen, R. E. *Solid State Nucl. Magn. Reson.* **2003**, *24*, 163–183.
- (55) Whuler, P. A.; Brouty, C.; Spinat, P.; Herpin, P. *Acta Crystallogr., Sect. B* **1975**, *130*, 145.
- (56) Nakatsu, K.; Saito, Y.; Kuroya, H. *Bull. Chem. Soc. Jpn.* **1956**, *29*, 428.
- (57) Rappe, A. K.; Casewit, C. J.; Colwell, K. S.; Goddard, W. A.; Skiff, W. M. *J. Am. Chem. Soc.* **1992**, *114*, 10024.
- (58) Casewit, C. J.; Colwell, K. S.; Rappe, A. K. *J. Am. Chem. Soc.* **1992**, *114*, 10046.
- (59) Casewit, C. J.; Colwell, K. S.; Rappe, A. K. *J. Am. Chem. Soc.* **1992**, *114*, 10035.
- (60) Rappe, A. K.; Colwell, K. S.; Casewit, C. J. *Inorg. Chem.* **1993**, *32*, 3438.
- (61) Jameson, C. J. *J. Chem. Phys.* **2002**, *116*, 8912–8929.
- (62) Jameson, C. J.; de Dios, A. C. *J. Chem. Phys.* **2002**, *116*, 3805–3821.
- (63) Jameson, C. J. *J. Am. Chem. Soc.* **2004**, *126*, 10450–10456.
- (64) Sears, D. N.; Demko, B. A.; Ooms, K. J.; Wasylishen, R. E.; Huang, Y. *Chem. Mater.* **2005**, *17*, 5481–5488.
- (65) Jameson, C. J.; Stueber, D. J. *J. Chem. Phys.* **2004**, *120*, 10200–10214.
- (66) Stueber, D.; Jameson, C. J. *J. Chem. Phys.* **2004**, *120*, 1560–1571.
- (67) Allen, M. P.; Tildesley, D. J. *Computer Simulations of Liquids*; Oxford: Oxford, U.K., 1987.
- (68) Jameson, C. J.; Jameson, A. K.; Baello, B. I.; Lim, H. M. *J. Chem. Phys.* **1994**, *100*, 5965.
- (69) Jameson, C. J.; Jameson, A. K.; Lim, H. M.; Baello, B. I. *J. Chem. Phys.* **1994**, *100*, 5977.
- (70) Mezei, M. *Mol. Phys.* **1980**, *40*, 901.
- (71) Norman, G. E.; Filinov, V. S. *High Temp.* **1969**, *7*, 216.
- (72) Jameson, C. J.; Jameson, A. K.; Kostikin, P.; Baello, B. I. *J. Chem. Phys.* **2000**, *112*, 323.
- (73) Aziz, R. A.; Slaman, M. J. *Mol. Phys.* **1986**, *57*, 825.
- (74) Sears, D. N.; Jameson, C. J. *J. Chem. Phys.* **2004**, *121*, 2151–2157.
- (75) Weil, J. A.; Buck, T.; Clapp, J. E. *Adv. Magn. Reson.* **1973**, *6*, 183.
- (76) Veeman, W. S. *Philos. Trans. R. Soc. London* **1981**, A299, 629.
- (77) Pulay, P.; Wolinsky, K.; Baker, J.; PQS, version 2.5; Parallel Quantum Solutions: Fayetteville, AK, <http://www.pqs-chem.com> sales@pqs-chem.com.
- (78) Ditchfield, R. *Mol. Phys.* **1974**, *27*, 789.
- (79) Pulay, P. *Adv. Chem. Phys.* **1987**, *69*, 241.
- (80) Wolinsky, K.; Hinton, J.; Pulay, P. *J. Am. Chem. Soc.* **1990**, *112*, 8251.
- (81) Becke, A. D. *J. Chem. Phys.* **1993**, *98*, 5648.
- (82) Partridge, H.; Faegri, J., K. NASA Technical Memorandum 103918; 1992.
- (83) Bishop, D. A.; Cybulski, S. M. *Chem. Phys. Lett.* **1993**, *211*, 255.
- (84) Bacskay, G. B. *Chem. Phys.* **1981**, *61*, 385.
- (85) Pulay, P. *J. Comput. Chem.* **1982**, *3*, 556.
- (86) Sears, D. R.; Klug, H. P. *J. Chem. Phys.* **1962**, *37*, 3002.
- (87) Campbell, K.; Kuehl, C. J.; Ferguson, M. J.; Stang, P. J.; Tykwinski, R. R. *J. Am. Chem. Soc.* **2002**, *124*, 7266.
- (88) Campbell, K.; Ooms, K. J.; Wasylishen, R. E.; Tykwinski, R. R. *Org. Lett.* **2005**, *7*, 3397.